ACSNANO
www.acsnano.org
ARTICLE

Size-Dependent Heating of Magnetic Iron Oxide Nanoparticles

Sheng Tong,[†] Christopher A. Quinto,[‡] Linlin Zhang,[†] Priya Mohindra,[‡] and Gang Bao*[,†,‡]

[†]Department of Bioengineering, Rice University, Houston, Texas 77005, United States

[‡]Department of Biomedical Engineering, Georgia Institute of Technology and Emory University, Atlanta, Georgia 30332, United States

Supporting Information

ABSTRACT: **The ability to generate heat under an alternating magnetic field (AMF) makes magnetic iron oxide nanoparticles (MIONs) an ideal heat source for biomedical applications including cancer thermoablative therapy, tissue preservation, and remote control of cell function. However, there is a lack of quantitative understanding of the mechanisms governing heat generation of MIONs, and the optimal nanoparticle size for magnetic fluid heating (MFH) applications. Here, we show that MIONs with large sizes (>20 nm) have a specific absorption rate (SAR) significantly higher than that predicted by the widely used linear theory of MFH. The heating efficiency of MIONs in both the superparamagnetic and ferromagnetic regimes increased with size, which can be accurately characterized with a modified dynamic hysteresis model. In particular, the 40 nm ferromagnetic nanoparticles have an SAR value approaching the theoretical limit under a clinically relevant AMF. An *in vivo* study further demonstrated that the 40 nm MIONs could effectively heat tumor tissues at a minimal dose. Our experimental results and theoretical analysis on nanoparticle heating offer important insight into the rationale design of MION-based MFH for therapeutic applications.**

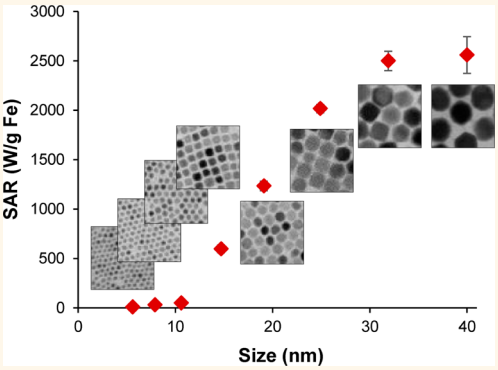

KEYWORDS: *iron oxide nanoparticles, magnetic fluid heating, Néelian relaxation, Brownian motion, hysteresis loss*

Upon exposure to an alternating magnetic field (AMF), magnetic nanoparticles (MNPs) dispersed in a solution can convert electromagnetic energy to heat, a phenomenon referred to as magnetic fluid heating (MFH).[1,2] This intriguing feature creates tremendous opportunities for the development of biomedical applications that can benefit from controlled supply of thermal energy to the tissue/organ. For example, focal heating of tumor tissues with MNPs delivered *in vivo* can increase the efficacy of cancer hyperthermia and thermoablative therapy.[3] MNPs fabricated with drug loading capacities have the potential to facilitate synergistic cancer hyperthermia and chemotherapy.[4] MNPs infused in tissue can provide homogeneous warming and improve tissue viability during the freeze–thaw cycle in organ preservation.[5,6] Recent studies have also shown that MNPs can regulate glucose metabolism or neuronal activities *in vivo via* heat-mediated signal transduction in cells.[7,8] A major challenge in the applications of MFH is the low heating efficiency of commercially available MNPs. The heating efficiency, characterized by specific absorption rate (SAR), of most MNPs reported to date ranges from a few to a few hundred watts per gram, making it difficult to reach the desired temperature at a relatively low dose of MNPs, as is the case in most therapeutic applications. Optimizing MFH for high heat induction is thus critical for developing nanoparticle heating-based therapeutics. Here, we present a comprehensive analysis of the size dependence of MFH, aiming to establish a better understanding of the mechanisms leading to efficient heat induction.

Heat induction of MNPs originates from the work done by an AMF exerted on nanocrystals, which depends on the AMF and the properties of MNPs. Although the heat generation of MNPs increases with the frequency (f) and the field strength (H) of AMF, a safety limit, $H{\cdot}f < 5 \times 10^9$ Am^{-1} S^{-1}, is empirically imposed on the AMF to avoid inducing eddy current in the body fluid in clinical applications.[9,10] It is, therefore, essential to increase the heating efficiency of MNPs by modulating their geometric and material properties under a clinically relevant AMF.[1,11−15] Among all magnetic materials, magnetic iron oxide nanoparticles (MIONs) have attracted the most attention owing to its biocompatibility in biomedical applications.[16] Theoretical analysis has shown that the heating efficiency of MIONs depends on their properties such as the saturation magnetization, anisotropy energy, and rate of magnetic relaxation.[1,15,17] For

Received: March 13, 2017
Accepted: June 17, 2017
Published: June 17, 2017

DOI: 10.1021/acsnano.7b01762
ACS Nano XXXX, XXX, XXX−XXX

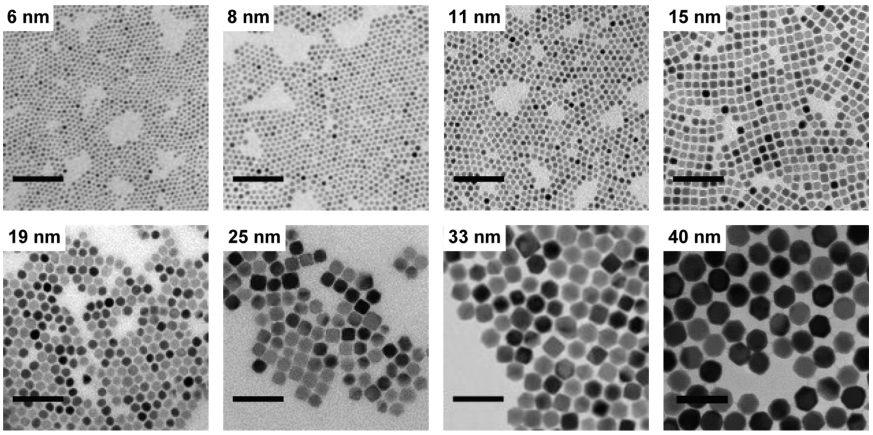

Figure 1. Transmission electron microscopy images of magnetic iron oxide nanocrystals. Scale bars equal 100 nm.

both magnetite (Fe_3O_4) and maghemite (γ-Fe_2O_3) nanoparticles, these properties are intrinsically associated with the size of nanocrystals.[18,19] In this regard, size is a controlling factor for increasing the heating efficiency of MIONs.

Over the last two decades, a number of theoretical and experimental studies have been focused on the size dependence of the heat induction of MIONs. In a cyclic AMF, the heat (A) generated by MIONs in each cycle can be written as

$$A = -\mu_0 \oint M dH \tag{1}$$

where μ_0 is the magnetic permeability of vacuum and M is the magnetization of MIONs. SAR can be calculated as the product of A and f. A can be obtained analytically with simplifying assumptions on the magnetic properties of MIONs. The most influential analytic solution for A was derived using a linear response theory (LRT) for superparamagnetic MIONs.[1] Assuming that the nanocrystals are uniaxial and of single magnetic domain, and the magnetic susceptibility is linearly proportional to the inductive field, LRT shows that

$$A = \mu_0 \pi H^2 \chi'' \tag{2}$$

$$\chi'' = \chi_0 \frac{2\pi f\tau}{1 + (2\pi f\tau)^2} \tag{2a}$$

where χ'' is the out-of-phase susceptibility, χ_0 is the equilibrium susceptibility, and τ is the relaxation time of MIONs determined by two size-dependent processes, Néel relaxation and rotational Brownian motion, represented by τ_N and τ_B, respectively ($1/\tau = 1/\tau_N + 1/\tau_B$).[1] Conversely, large ferromagnetic nanoparticles show magnetic hysteresis loops at room temperature, which are beyond the scope of the LRT model. The heat generation of ferromagnetic nanoparticles has been calculated from eq 1 using the Stoner–Wohlfarth model of hysteresis or the hysteresis loop measured experimentally.[15]

The LRT model has been widely accepted by the researchers in the field of MFH.[20] An important prediction of the LRT model is that MIONs attain the maximum heating efficiency when the relaxation time of MIONs approaches the period of AMF (see eq 2).[1,21] As a result, MIONs with ~14 nm diameter are predicted to be optimal with an AMF of 300 kHz, a frequency often used in MFH studies.[1,21] Numerous experimental studies on MION-induced MFH in the superparamagnetic size regime (≤20 nm) reported that the maximum SAR was achieved with MIONs of ~15 nm, whereas SAR decreased rapidly as the size either increased or decreased, consistent with the predicted trend using the LRT model.[12,19,21−25] These results, however, contradict with the fact that some of the highest SAR values were found with MIONs > 20 nm.[14,26] Further, the classic LRT model for MFH is based on certain assumptions of the magnetic properties of MIONs, which may not be applicable to MIONs with a wide range of sizes. Therefore, there is an unmet need for a better understanding of the size-dependent heat generation by MIONs and more robust design guideline for MFH with both superparamagnetic and ferromagnetic nanoparticles. Through a combined experimental study and theoretical analysis on heat generation by MIONs of 6−40 nm in size, we reveal that, contrary to the LRT model, the heating efficiency of MIONs increases with size far beyond 14 nm, and the 40 nm ferromagnetic nanoparticles have an SAR value approaching the theoretical limit under a clinically relevant AMF.

RESULTS

Synthesis of MIONs. The lack of systematic comparison of MFH in the superparamagnetic and ferromagnetic size regimes is mainly attributable to the difficulties in synthesizing MIONs of different size regimes with consistent conformation, uniform size distribution, and adequate aqueous dispersity. Here, we combined the thermodecomposition-based nanocrystal synthesis with a highly efficient dual solvent exchange coating method to generate MIONs with desirable properties (uniform size distribution, good aqueous dispersity, and reproducibility). It has been shown that magnetite nanocrystals with small size variations and high magnetic susceptibility can be synthesized through thermodecomposition of $Fe(acac)_3$ in a mixture of oleic acid, oleylamine, and long acyl chain diols in benzyl ether.[27,28] In this study, we utilized two synthesis methods to produce MIONs that cover superparamagnetic to ferromagnetic size regimes: nanocrystals with sizes of 6, 8, 11, and 15 nm were synthesized through seed-mediated growth;[27] those with sizes of 19, 25, 33, and 40 nm were synthesized using a similar method, but the ratio between oleic acid and oleylamine was increased to promote the growth of large crystals (Figure 1).[28] As-synthesized nanocrystals had a hydrophobic surface and were dispersed in toluene. The X-ray diffraction patterns of all nanocrystals are characteristic of the cubic spinel structure of magnetite (Supporting Figure S1).

Using the dual solvent exchange method,[29] we coated all the nanocrystals with amphiphilic copolymer DSPE-PEG2000, rendering them monodisperse in water (Table 1). To ensure consistent coating, the ratio between the DSPE-PEG2000 and

DOI: 10.1021/acsnano.7b01762
ACS Nano XXXX, XXX, XXX−XXX

Table 1. Properties of Magnetic Iron Oxide Nanoparticles

MION size	saturation magnetization, M_s (emu/g Fe)	core diameter (nm)	hydrodynamic diameter (nm)	polydispersity
6	107. 2	5.6 ± 0.9	21.2	0.01
8	109.2	7.9 ± 1.1	20.8	0.04
11	110.1	10.6 ± 1.0	19.5	0.05
15	117.3	14.7 ± 1.4	35.8	0.08
19	97.8	19.1 ± 1.6	32.4	0.11
25	115.3	24.9 ± 2.4	37.2	0.16
33	119.4	33.3 ± 4.0	48.2	0.14
40	116.1	40.4 ± 6.3	52.4	0.01

the surface area of the nanocrystals was fixed among all MIONs. The average size increase of MIONs after coating is consistent with the estimated size of DSPE-PEG2000.[30] The uniform thickness of the coating layer across nanocrystals with different sizes is advantageous for controlling the influence of Brownian relaxation on MFH.[1,31] Coated MIONs with core sizes of 6−19 nm remained well-dispersed in water for more than a year. In contrast, coated MIONs with core sizes of 25−40 nm showed a low level of precipitation after a few days of static storage, presumably due to their remanent magnetization and high density. However, precipitated MIONs could be dispersed by vortex, and redispersed MIONs showed similar size distribution in dynamic light scattering (DLS). We found that 40 nm was the size limit in synthesizing monodisperse MIONs using this method. Therefore, we opt to focus on MIONs of 6−40 nm in studying heating of monodisperse nanoparticles under AMF.

Magnetic Heating of MIONs. The heating efficiency of MIONs can be characterized by the specific absorption rate. For SAR measurement, MIONs dispersed in water were exposed to an alternating magnetic field generated by two different inductive coils at a fixed frequency (325 kHz). The average field strengths exerted on the ferrofluid were 20.7 and 9.35 kA/m according to numerical simulations, which yield $H{\cdot}f$ values of 6.7×10^9 and 3.0×10^9 Am^{-1} S^{-1} (Supporting Figure S2). The temperature of the ferrofluid was measured as a function of time, and the slopes of the heating profiles were used to calculate the SAR values (Supporting Figure S3). All MIONs showed nearly linear temperature increase with time, indicating that the effect of solution temperature on the heat induction was negligible. The 40 nm MIONs at a low concentration (0.5 mg Fe/mL) increased the solution temperature by more than 30 °C in 150 s, demonstrating extremely efficient heating for thermoablative therapy and other applications.

In sharp contrast to theoretical predictions using the LRT model, the measured SAR values of MIONs increased monotonically with nanocrystal size at both field strengths, and the most dramatic increases occurred between 11 and 33 nm, where SAR increased by ~50-fold (Figure 2A). SAR is very low for MIONs below 11 nm and reaches a plateau around 33−40 nm. With the 40 nm MIONs, the maximum SAR was found to be 1026 and 2560 W/(g Fe) at 9.35 and 20.7 kA/m field strength, respectively, which represents some of the highest SAR values measured to date.[22,32] The monotonic increase in SAR is in sharp contrast with previous findings that SAR decreased when the size of MIONs becomes >20 nm.[21,22,33] Guardia *et al.* reported that for iron oxide nanocubes, the relationship between edge length and SAR is dependent on the AMF field strength; a shift occurs between 12 and 24 kA/m, resulting in a large increase in SAR for 33 nm MIONs compared with smaller nanoparticles.[26] However, this phenomenon with nanocubes did not occur with the MIONs

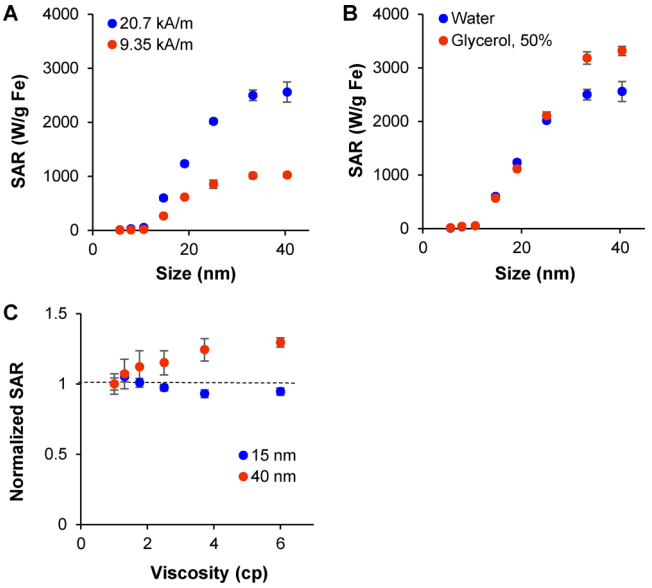

Figure 2. SAR measurements for MIONS of 6−40 nm in different solutions. The SAR values of MIONs were determined according to the temperature profiles in MFH experiments (see Supporting Figure S3). (A) SAR of MIONs dispersed in DI water with a field strength of 9.35 and 20.7 kA/m. The frequency of the AMF was fixed at 325 kHz. (B) SAR of MIONs dispersed in water *vs* 50% glycerol, measured under AMF of 20.7 kA/m and 325 kHz. (C) SAR of 15 and 40 nm MIONs dispersed in glycerol solutions at designated viscosity, measured under AMF of 20.7 kA/m and 325 kHz. Data represent mean ± standard deviation; n = 3 per group.

we synthesized because the trends of size dependence of SAR at 9.35 and 20.7 kA/m are similar (Figure 2A). By increasing the field strength from 9.35 to 20.7 kA/m, there was a 2.62-fold average increase in SAR, roughly corresponding to the increase in field strength (2.21-fold).

To examine the role of rotational Brownian relaxation in heat generation, we measured SAR for the MIONs dispersed in a high-viscosity solution of glycerol (Figure 2B) as higher viscosity may decrease the rotational Brownian relaxation of particles in solution.[21] Interestingly, for MIONs from 6 to 25 nm, SAR remained roughly the same in the glycerol solution, whereas for larger MIONs, SAR increased. These findings were further confirmed with a series of glycerol solutions with different viscosity (Figure 2C). Therefore, the SAR of large MIONs increased as the rotational Brownian relaxation decreased due to increased solvent viscosity. This finding contradicts with the LRT model which predicts that a 6-fold decrease in Brownian relaxation would dramatically reduce the out-of-phase susceptibility and thus the heat output (eq 2).

Magnetic Properties of MIONs. To gain a better understanding of the results shown in Figure 2 and establish a more comprehensive theoretical modeling of magnetic nanoparticle heating, we examined the size dependence of the equilibrium and dynamic magnetic properties of MIONs using a superconducting quantum interference device (SQUID). The nanocrystals were dispersed in a solid matrix of hexatriacontane in order to prevent the reorientation of nanocrystals and reduce interparticle interactions. As shown in Figure 3A, the magnetization curves measured at a magnetic field strength of up to 4×10^6 A/m have similar trends among MIONs with different sizes. The saturation magnetization (M_s) of the MIONs in each group synthesized (6−15 nm and 19−40 nm) increased slightly with

DOI: 10.1021/acsnano.7b01762
ACS Nano XXXX, XXX, XXX−XXX

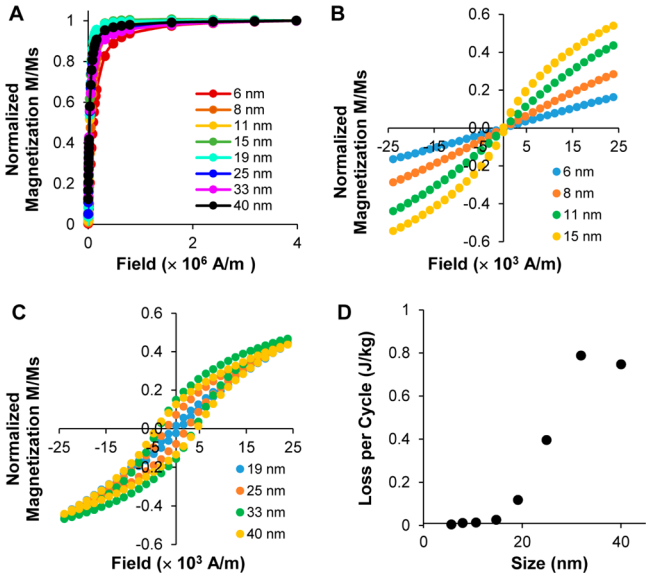

Figure 3. Equilibrium magnetic properties of MIONs. (A) Magnetization of MIONs measured from -4×10^6 to 4×10^6 A/m. Only the positive portions of the magnetization curves are shown in the plot. (B,C) Magnetization of MIONs measured within $\pm 25 \times 10^3$ A/m for MIONs of 6, 8, 11, and 15 nm (B) and MIONs of 19, 25, 33, and 40 nm (C). (D) Loss per cycle measured from magnetization curves shown in B and C according to eq 1.

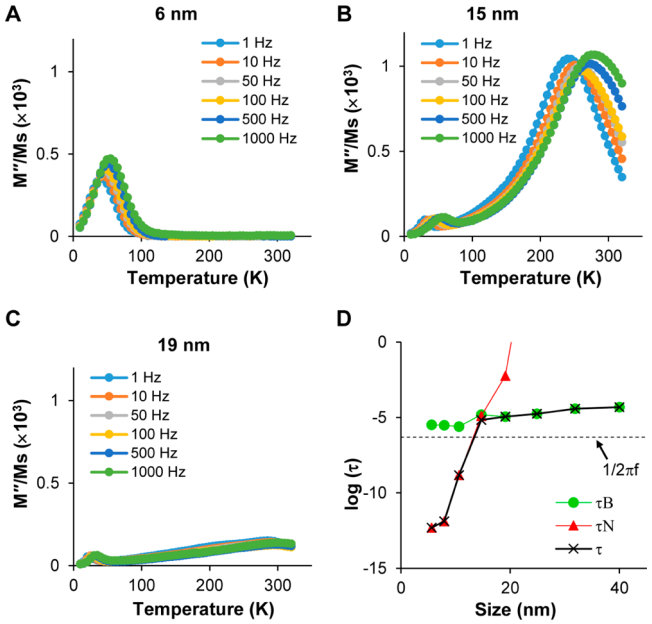

Figure 4. AC susceptibility of MIONs. AC susceptibility of MIONs of (A) 6, (B) 15, and (C) 19 nm core size, respectively. A complete set of AC susceptibility plots is given in Supporting Figure S7. (D) Néel relaxation time and Brownian relaxation time calculated using parameters derived from AC susceptibility and DLS measurements. The attempt time and the anisotropy energy constant of MIONs from 19 to 40 nm were assumed to be 10^{-12} S and 1.3×10^4 J/m^3, respectively. The dashed line marks the "ideal" relaxation time for an AMF of 325 kHz.

size (Table 1), which is typical of magnetite nanocrystals synthesized in the organic phase.[34] In most MFH studies, the dependence of magnetic response on the scanning field is overlooked. Here, we measured the magnetization curves of the nanocrystals at the same low field strength used in the SAR measurement. Indeed, the MIONs showed strongly size-dependent microhysteresis curves (Figure 3B,C). Specifically, 6−15 nm nanocrystals have negligible remanent magnetization, which is characteristic of superparamagnetic nanoparticles (Figure 3B). The susceptibility of the nanocrystals increased >3-fold as their size increased from 6 to 15 nm (Figure 3B). In contrast, the nanocrystals of 19−40 nm had hysteresis loops that widen with their size (Figure 3C). The shape of the microhysteresis curves indicates that the low field linear approximation in the LRT model is only valid for 6−11 nm MIONs. The coercivity and remanent magnetization also increased with the size of MIONs (Supporting Figure S4). The hysteresis loss per cycle calculated using eq 1 initially increases with size but reaches a plateau at 33 nm (Figure 3D). Further, the hysteresis loss per cycle increases with the field strength up to 48 kA/m (Supporting Figure S5). The zero-field-cooled (ZFC) and field-cooled (FC) magnetization curves show that the blocking temperature increases from 70 K for 6 nm MIONs to above room temperature when MION size is >15 nm (Supporting Figure S6).

AC susceptibility of the nanocrystals is often used to deduce the anisotropy constant and the out-of-phase magnetization (M″) in the LRT model. We found that the temperature at which the peak M″ occurs shifted toward higher temperature as the MION size increased from 6 to 15 nm (Figure 4A−C and Supporting Figure S7), whereas larger nanocrystals did not show recognizable peaks. The peak intensity increased when the size of MIONs increased from 6 to 15 nm with the exception of 8 nm but decreased drastically when MION size increased from 19 to 40 nm because the scanning field was smaller than the coercive field of the large nanocrystals. The anisotropy constant calculated using either the Néel law (6−11 nm) or Vogel−Fulcher law (15 nm) decreased from 1.9×10^5 to 2.1×10^4 J/m^3 with size, which is in good agreement with that reported in previous publications (Supporting Figure S8).[18,19] Note that the anisotropy constant includes the contributions from crystalline anisotropy, surface anisotropy, and shape anisotropy. In most published studies, the shape effect was implicitly included in the measured apparent anisotropic constant.[18,19] Likewise, we calculated the anisotropic constants of 6−15 nm MIONs based on the AC susceptibility measurements, which included the contribution of surface, crystallinity, and shape anisotropy. A number of studies have shown that the anisotropy constants of spherical *versus* cubic magnetic nanoparticles are similar.[14,35,36] Therefore, the variation in the anisotropy constant for the nanoparticles used in this study is mainly attributable to changes in their size. It is likely that the shape effect becomes significant only for nanoparticles with a large aspect ratio, such as nanorods. The anisotropic constants for large MIONs (>20 nm) could not be derived from the AC susceptibility measurements. As shown in several studies, the anisotropy constant of large nanoparticles approaches that of bulk magnetite, which is dominated by the crystalline anisotropy.[18,19] Therefore, we opted to use the anisotropy constant of bulk magnetite (1.35×10^4 J/m^3) for MIONs from 19 to 40 nm, which neglected the shape effect of large nanoparticles. The relaxation time was calculated for all MIONs using fitted attempt time, anisotropy constants, and the hydrodynamic diameter from DLS (Table 1). As shown in Figure 4D, Néel relaxation dominates for MIONs of 6−11 nm, whereas for MIONs of 15−40 nm, rotational Brownian relaxation has a significant contribution to the total relaxation time.

Comparison with Theoretical Models of MFH. To establish a better understanding of the size dependence of heat

DOI: 10.1021/acsnano.7b01762
ACS Nano XXXX, XXX, XXX−XXX

generation and to have a predictive model for MFH, the measured SAR values were compared to the predictions of several existing models (Figure 5B) at a field strength of 9.35 and 20.7 kA/m. Based on the LRT model, SAR is predominantly determined by the relaxation time because the saturation magnetization of all MIONs studied here are approximately the same (see eq 2). The LRT model predicts that among the MIONs we tested, the 15 nm MION is the only one that has a meaningful out-of-phase magnetization and has the largest SAR (Figure 5B, orange dashed line), which clearly contradicts with our SAR measurements shown in Figure 2A. The comparison between LRT model prediction and our experimental measurements in Figure 5B indicates that the LRT model is applicable only for iron oxide nanoparticles ≤15 nm. Further, using quasi-static hysteresis loops (Figure 3B,C), the SAR values calculated using eq 2 show a trend similar to the measured SAR except that the values are much lower (Figure 5B, green dashed line). It is clear that the LRT model fails to predict heating of MIONs not because of the difference between superparamagnetic and ferromagnetic nanoparticles but because of the linear assumption made. It is reasonable to assume that the LRT model is applicable for magnetic nanoparticles that respond linearly to the applied magnetic field.

Using a statistical physics approach, Carrey *et al.* established a dynamic hysteresis model (DHM) and showed that hysteresis changes with the field strength as well as the frequency of the magnetic field,[17] which is consistent with our experimental measurements (Supporting Figure S5). In particular, the hysteresis loop widens with frequency, as shown in the simulation for 19 nm MIONs, which explains the underestimation of SAR in the quasi-static hysteresis model (Supporting Figure S9B). It should be noted that, when the peak field strength equals 20 kA/m, numerical simulations using the DHM yield flat hysteresis loops for the 33 nm MIONs due to the extremely high energy barrier between different energy levels (Supporting Figure S9C). The simulations with a higher field strength (30 kA/m) showed a hysteresis loop wider than the one measured at the quasi-static condition (Figure 3C and Supporting Figure S9D). This reflects a fundamental limitation of the MFH models due to the assumption that nanoparticles are uniaxial with only two energy levels, which contradicts with the energy profile of the cubic spinel crystal of magnetite. Assuming the nondimensional parameter κ in the dynamic hysteresis model is less than 0.7 and the easy magnetic axis of the nanocrystals is aligned with the field, Carrey *et al.* provided the following empirical equation[17]

$$A = 1.92\mu_0 M_s H_k (1 - \kappa^{0.8}) \tag{3}$$

$$\kappa = \frac{k_B T}{K_A V} \ln\left(\frac{k_B T}{4\mu_0 M_s V H f \tau_0}\right) \tag{3a}$$

where $H_k = 2K_A/\mu_0 M_s$ is the anisotropy field, K_A the anisotropy constant, M_s the saturation magnetization, k_B the Boltzmann constant, T the temperature, V the volume of the nanocrystal, and τ_0 the attempt time, which is set at 10^{-10} s. Using the parameters obtained in this study, we found that $\kappa < 0.7$ implies that the MIONs are larger than 19 nm. In this size range, the DHM predictions are in good agreement with the measured SAR at 20.7 kA/m but not 9.35 kA/m (Figure 5B, orange dotted and purple dashed lines, respectively). This is due to the use of the anisotropy field in DHM which is a constant for each core size,

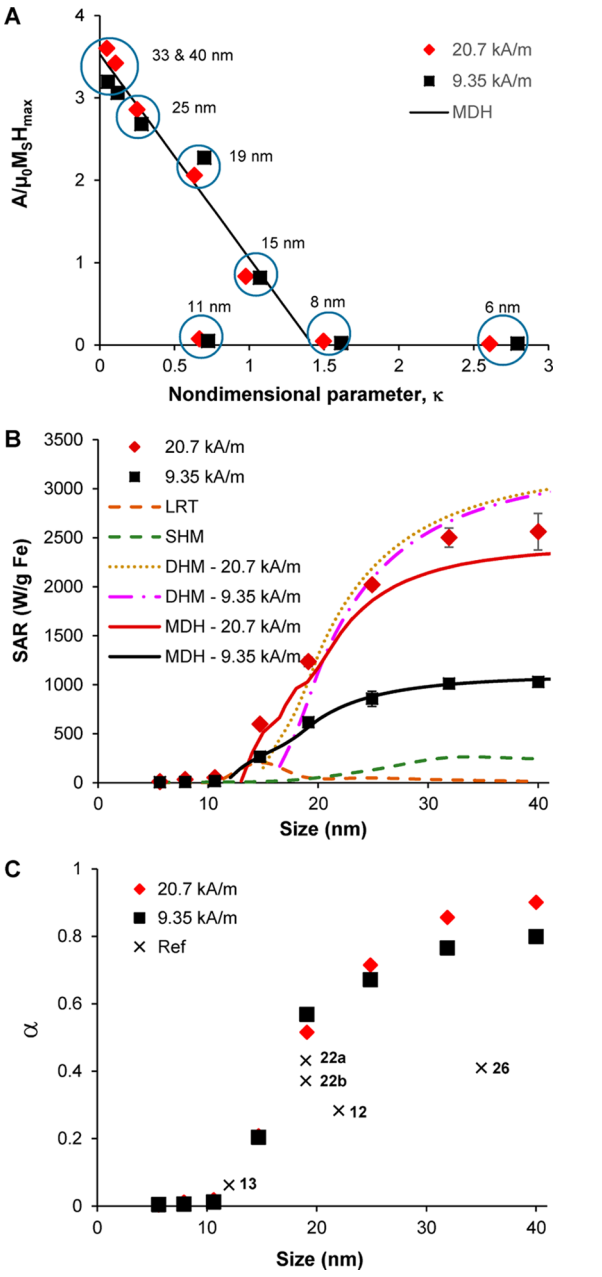

Figure 5. Comparison of model predictions and experimental results of the heat induction of MIONs. Experimental data were compared with theoretical predictions based on parameters derived from measurements of magnetic properties. (A) Plots showing the normalized hysteresis loss, $A/\mu_0 M_s H_{max}$, *vs* the nondimensional parameter κ calculated based on experimental data and a linear fitting for MIONs from 15 to 40 nm to establish a modified dynamic hysteresis (MDH) model. The point from the 11 nm MIONs was an outlier and excluded from the fitting. (B) Experimental measurements and theoretical predictions of SAR. LRT denotes the linear response theory. SHM denotes heat generation calculated using quasi-static hysteresis loops measured with SQUID at a scanning rate of approximately 30 min per cycle. The DHM curves are calculated based on a dynamic hysteresis model assuming the easy magnetic axis of the nanocrystals is aligned with the magnetic field (eq 3). The MDH curves are calculated based on the MDH model (eq 4). (C) Comparison of measured SAR in terms of a nondimensional parameter α calculated from SAR = $\alpha A_{max} f$. The numbers in the plot indicate the cited references (Supporting Table S1).

DOI: 10.1021/acsnano.7b01762
ACS Nano XXXX, XXX, XXX−XXX

giving rise to underestimation of the dependence of SAR on the field strength.

To obtain a better predictive model for SAR for MIONs in clinically relevant AMF, we plotted $A/\mu_0 M_s H_{max}$ as a function of κ using the material properties and SAR values measured experimentally in this study. As can be seen from Figure 5A, there is a linear dependence on κ for MIONs from 15 to 40 nm at both field strengths (9.35 and 20.7 kA/m). We thus established a modified dynamic hysteresis (MDH) model based on the linear fitting

$$A = 3.53\mu_0 M_s H_{max}(1 - 0.7\kappa) \quad (4)$$

and found that the MDH model is in good agreement with our SAR measurements for MIONs ≥15 nm at both field strengths (Figure 5B). Note that the values of κ for 33 and 40 nm MIONs are 0.104 and 0.047, respectively. Note also that A in eq 4 reaches its maximum $3.53\mu_0 M_s H_{max}$ when $\kappa = 0$, which is fully determined by the saturation magnetization of MIONs M_s and the maximum field strength H_{max} of AMF and sets the limit for designing MFH applications. Our MDH model indicates that the SAR values of 33 and 40 nm MIONs are, respectively, 92.7 and 96.7% of the maximum SAR value at 20.7 kA/m and 325 kHz. It implies that for MIONs with single magnetic domain, further increasing the size will not lead to significant gain in the heating efficiency.

For all magnetic nanoparticles, the hysteresis loop is confined by a rectangle defined by M_s and H_{max}, which yields a theoretical magnetic heating limit of $A_{max} = 4\mu_0 M_s H_{max}$.[17] Shown in Figure 5C and Supporting Table S1 are the experimentally measured SAR values for MIONs studied here as well as those with the highest SAR reported elsewhere,[12,13,22,26] expressed in terms of a nondimensional parameter α, defined by SAR = $\alpha A_{max} f$. Note that $\alpha = 1$ represents the theoretical magnetic heating limit. For MIONs smaller than 20 nm, the α values obtained in this study are consistent with that from previous studies.[12,13] However, there is a large discrepancy when the MIONs are larger than 20 nm. In a pilot study, we found that the aggregated 33 nm ferromagnetic MIONs had an SAR value less than 1/3 of that of the well-dispersed counterpart (data not shown), which may explain why much lower SAR values were reported for ferromagnetic MIONs. Importantly, the α values of MIONs synthesized in this study increase with size and approach 0.88 (with a field strength of 20.7 kA/m), close to the theoretical limit of 1.0. Although SAR measurements exist on MIONs having heterogeneous size distributions, such as EMG308 (ferrofluid.ferrotec.com) and Micromod (www.micromod.de), we did not include them in Figure 5C due to the requirement of MION monodispersity in this study.

***In Vivo* Tumor Heating.** To illustrate the potential applications of MFH, we tested three MIONs encompassing the size range in this study (6, 19, 40 nm) using a mouse xenograft tumor model for glioblastoma multiforme (GBM). GBM is an aggressive and invasive brain cancer of which surgical resection is difficult to perform, and thus alternative treatment strategies such as local hyperthermia/thermoablative therapy are sought after.[37] The tumor tissue represents a heterogeneous microenvironment for MFH due to the complex tissue structure and homeostatic temperature regulation mechanisms. U87 tumors grown subcutaneously were injected intratumorally with 50 μg of Fe of MIONs. T_2-weighted magnetic resonance (MR) images acquired before and after injection display the sharp contrast of the MIONs inside the tumor, which could provide an estimate of the affected region (Figure 6A and Supporting Figure S10). Note that T_2-weighted MR contrast

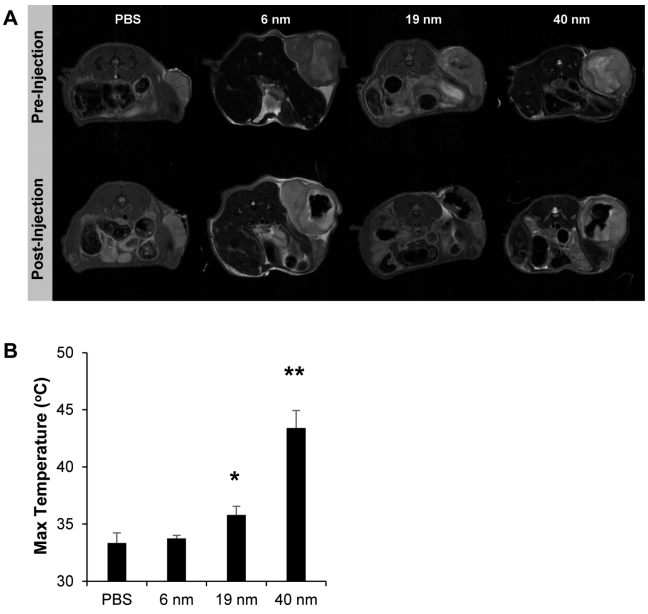

Figure 6. *In vivo* MFH in tumor tissue. Phosphate-buffered saline or solutions containing 50 μg of Fe/mL of MIONs were infused into the center of U87 tumors on the flank of mice. MFH was applied for 1 h at 9.35 kA/m and 325 kHz. (A) MRI images of the cross section of the mouse bodies before and after infusion of MION solution. (B) Maximum temperature reached during 1 h of heating. For complete temperature profiles, see Supporting Figure S12. Data represent mean ± SEM; $n = 4$ per group; *$p < 0.05$ and **$p < 0.01$ according to one-way Student's t test.

would saturate at a concentration above 0.1 mg Fe/mL.[38] A more accurate dosimetry of the spatial temperature profiles during MFH treatment can be obtained by *in vivo* quantitative MR imaging of MIONs.[39,40] Following imaging, the mice were exposed to an AMF (9.35 kA/m, 325 kHz) for 1 h (Supporting Figure S11). The tumors injected with the 6 nm MIONs did not exhibit a temperature increase compared to the control, whereas the 19 and 40 nm MIONs generated a temperature increase of 2.5 and 10.1 °C, respectively (Figure 6B and Supporting Figure S12). The increases in the temperature attained *in vivo* correspond well with the SAR values measured in solution. The 40 nm MIONs were able to reach 43.4 ± 1.5 °C during the course of the treatment, which suffices the temperature requirement of many cancer thermal therapies.[41,42] We were able to achieve substantial *in vivo* heating using only 50 μg of MIONs and an AMF of 9.35 kA/m at 325 kHz, much lower than that used in previous studies (*e.g.*, with a few milligrams of irons or with field strengths up to 56 kA/m).[43−45] Note the measurements only reflect the bulk temperature of the tumor. The cellular uptake of nanoparticles is size-dependent, which could affect the intratumoral distribution of MIONs and consequently the therapeutic outcome of heating.[46] Nevertheless, our promising *in vivo* results set the stage for designing an effective magnetic nanoparticle-based strategy for MFH thermotherapy of cancer.

CONCLUSIONS

We present a systematic study of the size dependence of heat generation by magnetic iron oxide nanoparticles under AMF. Through careful measurement of the equilibrium and dynamic magnetic properties of MIONs, we analyzed the mechanisms governing MFH of MIONs with different sizes, compared our

DOI: 10.1021/acsnano.7b01762
ACS Nano XXXX, XXX, XXX−XXX

SAR measurements with different MFH theories, and identified the optimal MION size. Our results suggest that Brownian motion is not a major contributing factor in MFH, and there is a nonlinear dependence of the hysteresis on the frequency and field strength of the applied AMF, consistent with the dynamic hysteresis model of MFH. In particular, monodisperse MIONs larger than 20 nm are more effective in heat induction, contrary to the widely accepted prediction by the LRT model. In particular, 14 nm is not the optimal nanoparticle size for magnetic heating, suggesting that the linear theory developed by Rosensweig[1] is not accurate for predicting the heating efficiency of MIONs, be they ferromagnetic or superparamagnetic (>14 nm). Through combined experimental and theoretical analysis, we derived a more accurate phenomenological model for SAR under a clinically relevant AMF. These findings have significant implications on engineering MIONs for biomedical applications of MFH.

METHODS

Chemicals. Iron acetylacetonate ($Fe(acac)_3$ 99%), 1,2-tetradecanediol (technical grade, 90%), oleic acid (technical grade, 90%), oleylamine (technical grade, 70%), benzyl ether (98%), hydrochloric acid (>37%), hydroxylamine HCl, sodium hydroxide, ammonium acetate, ferrozine, and iron standard (1000 mg/L Fe in nitric acid) were purchased from Sigma-Aldrich and used as received. 1,2-Distearoyl-*sn*-glycero-3-phosphoethanolamine-*N*-[methoxy(polyethylene glycol)-2000] (ammonium salt) (DSPE-PEG2000) were purchased from Avanti Polar Lipids.

Synthesis of Magnetite Nanocrystals. Magnetite nanocrystals were synthesized by thermodecomposition of iron acetylacetonate using the protocols established according to the literature.[27,28] To synthesize the nanocrystals of 6 nm in diameter, a mixture of iron acetylacetonate (12 mmol), 1,2-tetradecanediol (60 mmol), oleic acid (72 mmol), oleylamine (72 mmol), and 60 mL of benzyl ether was incubated at 100 °C for 1 h under vacuum. Then, the solution was heated at 200 °C for 2 h and at 300 °C for 1 h with argon flow. The temperature ramping rate was set at 5 °C/min among steps. After the reaction, the nanocrystals were collected by repeated precipitation with ethanol and dispersion with toluene. Highly uniform nanocrystals (<15 nm) could be synthesized by sequential seed-mediated growth from the 6 nm nanocrystals. In each step, small nanocrystals were mixed with iron acetylacetonate (6 mmol), 1,2-tetradecanediol (30 mMol), oleic acid (18 mMol), and oleylamine (18 mMol) in 60 mL of benzyl ether and the heating at 200 and 300 °C was reduced to 1 h and 30 min, respectively. The size increase in each step was determined by the iron ratio between the seeds and the precursor compound.

Larger nanocrystals (19−40 nm) were obtained by reducing the iron precursor concentration, increasing the ratio between oleic acid and oleylamine, and reducing the temperature ramping rate from 200 to 300 °C. In a typical synthesis, iron acetylacetonate (6 mmol), 1,2-tetradecanediol (24 mmol), oleic acid (48 mmol), and oleylamine (12 mMol) were mixed in 60 mL of benzyl ether. Heating at 200 and 300 °C were maintained for 30 and 120 min, respectively. The ramping rate was set between 2 and 5 °C/min with slower ramping facilitating the formation of larger nanocrystals.

Characterization of Nanocrystals. The size, structure, and magnetic properties of the nanocrystals were characterized by transmission electron microscopy (TEM), X-ray diffraction (XRD), and SQUID magnetometry. TEM images were acquired using a transmission electron microscope (Hitachi H-7500) connected to a CCD camera. TEM procedures were conducted by the Robert P. Apkarian Integrated Electron Microscopy Core at Emory University. The average diameter of the nanocrystals was measured using an image processing software (ImagePro Plus). For XRD measurement, the nanocrystals dispersed in toluene were precipitated with ethanol and dried under vacuum overnight. Powder XRD measurements were performed with an X-ray diffractometer (Rigaku SmartLab).

Magnetic properties were measured using a superconducting quantum interference device (Quantum Design MPMS). The nanocrystals were dispersed in hexatriacontane at a weight ratio of approximately 5% to prevent sample movement and to reduce magnetic coupling among the nanocrystals. The equilibrium magnetization of the nanocrystals was measured from -4×10^6 to 4×10^6 A/m at 300 K. The microhysteresis of the nanocrystals was measured from −23.8 to 23.8 kA/m at 300 K. Zero-field-cooled and field-cooled measurements were performed with a magnetic field of 796 A/m (10 Oe). AC susceptibility was measured from 1 to 1000 Hz within a temperature range of 10 to 320 K and with a magnetic field of 332 A/m (4 Oe). To calculate the mass magnetization accurately, the iron content of the samples was directly measured from the pellets after the measurements. In brief, the pellets were digested with 5 mL of 12 M hydrochloric acid, and the iron concentration of the solutions was measured by a ferrozine assay.

Synthesis of Water-Dispersible Magnetic Iron Oxide Nanoparticles. As-synthesized nanocrystals were dispersed in toluene. Water-dispersible MNPs were synthesized by coating the nanocrystals with an amphiphilic copolymer, DSPE-PEG, through a dual solvent exchange procedure described previously.[29] In brief, the nanocrystals were mixed with 20 mg of DSPE-PEG in chloroform. The amount of the nanocrystals was determined based on a ratio of 4 DSPE-PEG molecules/nm^2 surface area of the nanocrystals. Twenty milliliters of DMSO was incrementally added to the mixture, followed by removal of toluene and chloroform *via* vaporization. After that, 32 mL of deionized water was slowly added to the solution. DMSO was removed through two rounds of centrifugation in centrifugal filter tubes (Vivaspin 20, 100 kDa cutoff size). Free DSPE-PEG in the solution was further removed by two rounds of ultracentrifugation. Finally, the solution was passed through a 0.2 μm syringe filter and stored at 4 °C. The hydrodynamic diameter of the MIONs was measured by dynamic light scattering (DynaPro Nanostar, Wyatt Technology). The mass-weighted diameter and polydispersity index were reported.

Iron Concentration Measurement. The iron content of samples was determined using a ferrozine assay. Briefly, 50 μL of sample was mixed with 50 μL of 12 M HCl and incubated at room temperature for 10 min. Then, 240 μL of 2 M NaOH, 50 μL of 4 M ammonium acetate, 110 μL of 5% hydroxylamine HCl, and 500 μL of water were added to the solution sequentially. After 30 min of incubation, 50 μL of the solution was mixed with 0.01% ferrozine solution in a 384-well plate. Light absorption was read at 562 nm with 810 nm as the reference wavelength using a microplate reader. The iron concentration was determined by comparison to a standard curve created with an iron standard.

Magnetic Fluid Heating. The magnetic fluid heating experiments were conducted with a 1 kW EASYHEAT induction heating system (Ameritherm), which could generate an AMF at a fixed frequency (325 kHz). The system was equipped with two coils that were either 7.5-turn, 2.54 cm inner diameter or 5-turn, 5.00 cm inner diameter. The height of both coils was 3 cm. The peak field strengths of the AMF generated by the two coils were 23.8 and 13.3 kA/m as reported by the manufacturer. The distribution of the magnetic field and the average field strength exerted on the sample were computed using a mathematic model developed with the Comsol Multiphysics software (Supporting Figure S2).

For the SAR measurement, 1.5 mL of MIONs dispersed in designated solvents was added to a 2 mL of cryovial insulated with Styrofoam. The cryovial was placed in the center of the inductive coil, and the induction heating system was turned on for 150 s. The temperature increase in the solution was recorded in real time with a fiber-optic temperature probe (Lumasense m3300). The experiment was carried out under close to adiabatic conditions. The average slope of the temperature *versus* time plot during the first 20 s of heating was calculated by forward linear fitting for each sample and subtracted by that of the solvent alone to compensate for the heat exchange with the environment. SAR was calculated with the following equation

$$\mathrm{SAR} = \frac{1}{m_{\mathrm{Fe}}} C_{\mathrm{sol}} m_{\mathrm{sol}} \left(\frac{\mathrm{d}T}{\mathrm{d}t} \right) \tag{5}$$

DOI: 10.1021/acsnano.7b01762
ACS Nano XXXX, XXX, XXX−XXX

where m_{Fe} is the mass of the iron in the sample, C_{sol} is the specific heat of the solvent (C_{H_2O} = 4.184 J K^{-1} g^{-1}, $C_{glycerol}$ = 2.41 J K^{-1} g^{-1}), m_{sol} is the mass of the solvent, and dT/dt is the slope of the temperature *versus* time. To evaluate the effect of Brownian motion on heating, SAR was measured for the MIONs dispersed in a series of glycerol solutions. The glycerol solutions were generated by mixing glycerol with water at designed weight ratios. The specific heat of the resulting solutions were calculated as the averaged specific heat of glycerol and water based on the weight ratio.[47] The viscosities of the solutions were reported in a previous publication.[48]

***In Vivo* Tumor Hyperthermia.** All animal procedures were approved by the Institutional Animal Care and Use Committee at the Georgia Institute of Technology. Female athymic nude mice 4−5 weeks old were purchased from Charles River. U87 glioblastoma cells were purchased from ATCC and cultured according to the distributor's instructions. Xenograft tumors were induced in nude mice by subcutaneous injection of 3 × 10^6 U87 cells into the right flank. Tumors were monitored until reaching ∼500 mm^3 in size. The mice were anesthetized with 1.5% isoflurane and injected with 10 μL of either 6, 19, or 40 nm MIONs (50 μg Fe) or saline intratumorally over 10 min using a syringe pump. The mice were placed on a polycarbonate mouse cradle inside an inductive coil (5 turns, 5.00 cm inner diameter) with the tumor centered with the coil in the axial direction (Supporting Figure S11). A fiber-optic temperature probe was bluntly inserted into the center of the tumor. The animal was then exposed to an AMF (9.35 kA/m, 325 kHz) for 1 h while recording the intratumoral temperature. MR imaging was performed using a Bruker 7 T small animal MRI instrument with a 38 mm coil (Pharmascan, Bruker). Images were acquired using a spin−echo sequence (TR = 2000 ms; TE = 13.5 ms; matrix size = 256 × 256, FOV = 30 mm) before and after intratumoral injection of MIONs and following the 1 h AMF treatment.

ASSOCIATED CONTENT

Supporting Information

The Supporting Information is available free of charge on the ACS Publications website at DOI: 10.1021/acsnano.7b01762.

XRD patterns of iron oxide nanocrystals; inductive coils used in SAR measurements; heating profiles of MIONs in water; equilibrium magnetic properties of iron oxide nanocrystals; dependence of hysteresis of MIONs on field strength; ZFC and FC curves of iron oxide nanocrystals; AC susceptibility of iron oxide nanocrystals; anisotropy constants of iron oxide nanocrystals; simulated dynamic hysteresis loops; MR images of mouse cross sections; *in vivo* MFH set up; *in vivo* tumor heating profiles; a table of SAR and α values of MIONs used in this study and cited references (PDF)

AUTHOR INFORMATION

Corresponding Author

*E-mail: gang.bao@rice.edu.

ORCID

Sheng Tong: 0000-0001-8632-7933

Gang Bao: 0000-0001-5501-554X

Notes

The authors declare no competing financial interest.

ACKNOWLEDGMENTS

This work was supported by the Cancer Prevention and Research Institute of Texas (RR140081 to G.B.).

REFERENCES

(1) Rosensweig, R. E. Heating Magnetic Fluid with Alternating Magnetic Field. *J. Magn. Magn. Mater.* **2002**, *252*, 370−374.

(2) Mornet, S.; Vasseur, S.; Grasset, F.; Duguet, E. Magnetic Nanoparticle Design for Medical Diagnosis and Therapy. *J. Mater. Chem.* **2004**, *14*, 2161−2175.

(3) Kumar, C. S.; Mohammad, F. Magnetic Nanomaterials for Hyperthermia-Based Therapy and Controlled Drug Delivery. *Adv. Drug Delivery Rev.* **2011**, *63*, 789−808.

(4) Quinto, C. A.; Mohindra, P.; Tong, S.; Bao, G. Multifunctional Superparamagnetic Iron Oxide Nanoparticles for Combined Chemotherapy and Hyperthermia Cancer Treatment. *Nanoscale* **2015**, *7*, 12728−12736.

(5) Etheridge, M. L.; Xu, Y.; Rott, L.; Choi, J.; Glasmacher, B.; Bischof, J. C. RF Heating of Magnetic Nanoparticles Improves the Thawing of Cryopreserved Biomaterials. *TECHNOLOGY* **2014**, *02*, 229−242.

(6) Manuchehrabadi, N.; Gao, Z.; Zhang, J.; Ring, H. L.; Shao, Q.; Liu, F.; McDermott, M.; Fok, A.; Rabin, Y.; Brockbank, K. G.; Garwood, M.; Haynes, C. L.; Bischof, J. C. Improved Tissue Cryopreservation Using Inductive Heating of Magnetic Nanoparticles. *Sci. Transl. Med.* **2017**, *9*, eaah4586.

(7) Stanley, S. A.; Gagner, J. E.; Damanpour, S.; Yoshida, M.; Dordick, J. S.; Friedman, J. M. Radio-Wave Heating of Iron Oxide Nanoparticles Can. Regulate Plasma Glucose in Mice. *Science* **2012**, *336*, 604−608.

(8) Leibiger, I. B.; Berggren, P. O. Regulation of Glucose Homeostasis Using Radiogenetics and Magnetogenetics in Mice. *Nat. Med.* **2015**, *21*, 14−16.

(9) Hergt, R.; Dutz, S. Magnetic Particle Hyperthermia-Biophysical Limitations of a Visionary Tumour Therapy. *J. Magn. Magn. Mater.* **2007**, *311*, 187−192.

(10) Brezovich, I. A. Low Frequency Hyperthermia: Capacitive and Ferromagnetic Thermoseed Methods. *Med. Phys. Monograph* **1988**, *16*, 82−111.

(11) Jang, J. T.; Nah, H.; Lee, J. H.; Moon, S. H.; Kim, M. G.; Cheon, J. Critical Enhancements of Mri Contrast and Hyperthermic Effects by Dopant-Controlled Magnetic Nanoparticles. *Angew. Chem., Int. Ed.* **2009**, *48*, 1234−1238.

(12) Chen, R.; Christiansen, M. G.; Anikeeva, P. Maximizing Hysteretic Losses in Magnetic Ferrite Nanoparticles *via* Model-Driven Synthesis and Materials Optimization. *ACS Nano* **2013**, *7*, 8990−9000.

(13) Lee, J. H.; Jang, J. T.; Choi, J. S.; Moon, S. H.; Noh, S. H.; Kim, J. W.; Kim, J. G.; Kim, I. S.; Park, K. I.; Cheon, J. Exchange-Coupled Magnetic Nanoparticles for Efficient Heat Induction. *Nat. Nanotechnol.* **2011**, *6*, 418−422.

(14) Noh, S. H.; Na, W.; Jang, J. T.; Lee, J. H.; Lee, E. J.; Moon, S. H.; Lim, Y.; Shin, J. S.; Cheon, J. Nanoscale Magnetism Control *via* Surface and Exchange Anisotropy for Optimized Ferrimagnetic Hysteresis. *Nano Lett.* **2012**, *12*, 3716−3721.

(15) Hergt, R.; Dutz, S.; Roder, M. Effects of Size Distribution on Hysteresis Losses of Magnetic Nanoparticles for Hyperthermia. *J. Phys.: Condens. Matter* **2008**, *20*, 385214.

(16) Bao, G.; Mitragotri, S.; Tong, S. Multifunctional Nanoparticles for Drug Delivery and Molecular Imaging. *Annu. Rev. Biomed. Eng.* **2013**, *15*, 253−282.

(17) Carrey, J.; Mehdaoui, B.; Respaud, M. Simple Models for Dynamic Hysteresis Loop Calculations of Magnetic Single-Domain Nanoparticles: Application to Magnetic Hyperthermia Optimization. *J. Appl. Phys.* **2011**, *109*, 083921.

(18) Demortiere, A.; Panissod, P.; Pichon, B. P.; Pourroy, G.; Guillon, D.; Donnio, B.; Begin-Colin, S. Size-Dependent Properties of Magnetic Iron Oxide Nanocrystals. *Nanoscale* **2011**, *3*, 225−232.

(19) Lartigue, L.; Innocenti, C.; Kalaivani, T.; Awwad, A.; Sanchez Duque, M.; Guari, Y.; Larionova, J.; Guerin, C.; Montero, J. L.; Barragan-Montero, V.; Arosio, P.; Lascialfari, A.; Gatteschi, D.; Sangregorio, C. Water-Dispersible Sugar-Coated Iron Oxide Nanoparticles. An Evaluation of Their Relaxometric and Magnetic Hyperthermia Properties. *J. Am. Chem. Soc.* **2011**, *133*, 10459−10472.

(20) Deatsch, A. E.; Evans, B. A. Heating Efficiency in Magnetic Nanoparticle Hyperthermia. *J. Magn. Magn. Mater.* **2014**, *354*, 163−172.

(21) Fortin, J. P.; Wilhelm, C.; Servais, J.; Menager, C.; Bacri, J. C.; Gazeau, F. Size-Sorted Anionic Iron Oxide Nanomagnets as Colloidal

DOI: 10.1021/acsnano.7b01762
ACS Nano XXXX, XXX, XXX−XXX

Mediators for Magnetic Hyperthermia. *J. Am. Chem. Soc.* **2007**, *129*, 2628−2635.
(22) Guardia, P.; Di Corato, R.; Lartigue, L.; Wilhelm, C.; Espinosa, A.; Garcia-Hernandez, M.; Gazeau, F.; Manna, L.; Pellegrino, T. Water-Soluble Iron Oxide Nanocubes with High Values of Specific Absorption Rate for Cancer Cell Hyperthermia Treatment. *ACS Nano* **2012**, *6*, 3080−3091.
(23) Vreeland, E. C.; Watt, J.; Schober, G. B.; Hance, B. G.; Austin, M. J.; Price, A. D.; Fellows, B. D.; Monson, T. C.; Hudak, N. S.; Maldonado-Camargo, L.; Bohorquez, A. C.; Rinaldi, C.; Huber, D. L. Enhanced Nanoparticle Size Control by Extending Lamer's Mechanism. *Chem. Mater.* **2015**, *27*, 6059−6066.
(24) Levy, M.; Quarta, A.; Espinosa, A.; Figuerola, A.; Wilhelm, C.; Garcia-Hernandez, M.; Genovese, A.; Falqui, A.; Alloyeau, D.; Buonsanti, R.; Cozzoli, P. D.; Garcia, M. A.; Gazeau, F.; Pellegrino, T. Correlating Magneto-Structural Properties to Hyperthermia Performance of Highly Monodisperse Iron Oxide Nanoparticles Prepared by a Seeded-Growth Route. *Chem. Mater.* **2011**, *23*, 4170−4180.
(25) Gonzales-Weimuller, M.; Zeisberger, M.; Krishnan, K. M. Size-Dependant Heating Rates of Iron Oxide Nanoparticles for Magnetic Fluid Hyperthermia. *J. Magn. Magn. Mater.* **2009**, *321*, 1947−1950.
(26) Guardia, P.; Riedinger, A.; Nitti, S.; Pugliese, G.; Marras, S.; Genovese, A.; Materia, M. E.; Lefevre, C.; Manna, L.; Pellegrino, T. One Pot Synthesis of Monodisperse Water Soluble Iron Oxide Nanocrystals with High Values of the Specific Absorption Rate. *J. Mater. Chem. B* **2014**, *2*, 4426−4434.
(27) Sun, S.; Zeng, H.; Robinson, D. B.; Raoux, S.; Rice, P. M.; Wang, S. X.; Li, G. Monodisperse Mfe2o4 (M = Fe, Co, Mn) Nanoparticles. *J. Am. Chem. Soc.* **2004**, *126*, 273−279.
(28) Yang, H.; Ogawa, T.; Hasegawa, D.; Takahashi, M. Synthesis and Magnetic Properties of Monodisperse Magnetite Nanocubes. *J. Appl. Phys.* **2008**, *103*, 07D526.
(29) Tong, S.; Hou, S.; Ren, B.; Zheng, Z.; Bao, G. Self-Assembly of Phospholipid-Peg Coating on Nanoparticles through Dual Solvent Exchange. *Nano Lett.* **2011**, *11*, 3720−3726.
(30) Johnsson, M.; Hansson, P.; Edwards, K. Spherical Micelles and Other Self-Assembled Structures in Dilute Aqueous Mixtures of Poly(Ethylene Glycol) Lipids. *J. Phys. Chem. B* **2001**, *105*, 8420−8430.
(31) Tong, S.; Hou, S.; Zheng, Z.; Zhou, J.; Bao, G. Coating Optimization of Superparamagnetic Iron Oxide Nanoparticles for High T2 Relaxivity. *Nano Lett.* **2010**, *10*, 4607−4613.
(32) Hergt, R.; Hiergeist, R.; Zeisberger, M.; Schüler, D.; Heyen, U.; Hilger, I.; Kaiser, W. A. Magnetic Properties of Bacterial Magnetosomes as Potential Diagnostic and Therapeutic Tools. *J. Magn. Magn. Mater.* **2005**, *293*, 80−86.
(33) Martinez-Boubeta, C.; Simeonidis, K.; Makridis, A.; Angelakeris, M.; Iglesias, O.; Guardia, P.; Cabot, A.; Yedra, L.; Estrade, S.; Peiro, F.; Saghi, Z.; Midgley, P. A.; Conde-Leboran, I.; Serantes, D.; Baldomir, D. Learning from Nature to Improve the Heat Generation of Iron-Oxide Nanoparticles for Magnetic Hyperthermia Applications. *Sci. Rep.* **2013**, *3*, 1652.
(34) Guardia, P.; Labarta, A.; Batlle, X. Tuning the Size, the Shape, and the Magnetic Properties of Iron Oxide Nanoparticles. *J. Phys. Chem. C* **2011**, *115*, 390−396.
(35) Song, Q.; Zhang, Z. J. Shape Control and Associated Magnetic Properties of Spinel Cobalt Ferrite Nanocrystals. *J. Am. Chem. Soc.* **2004**, *126*, 6164−6168.
(36) Kovalenko, M. V.; Bodnarchuk, M. I.; Lechner, R. T.; Hesser, G.; Schaffler, F.; Heiss, W. Fatty Acid Salts as Stabilizers in Size- and Shape-Controlled Nanocrystal Synthesis: The Case of Inverse Spinel Iron Oxide. *J. Am. Chem. Soc.* **2007**, *129*, 6352−6353.
(37) Silva, A. C.; Oliveira, T. R.; Mamani, J. B.; Malheiros, S.; Malavolta, L.; Pavon, L. F.; Sibov, T. T.; Amaro, E., Jr.; Tannus, A.; Vidoto, E.; Matins, M. J.; Santos, R. S.; Gamarra, L. Application of Hyperthermia Induced by Superparamagnetic Iron Oxide Nanoparticles in Glioma Treatment. *Int. J. Nanomed.* **2011**, *6*, 591−603.
(38) Gneveckow, U.; Jordan, A.; Scholz, R.; Bruss, V.; Waldofner, N.; Ricke, J.; Feussner, A.; Hildebrandt, B.; Rau, B.; Wust, P. Description and Characterization of the Novel Hyperthermia- and Thermoablation-System Mfh 300f for Clinical Magnetic Fluid Hyperthermia. *Med. Phys.* **2004**, *31*, 1444−1451.
(39) Gharagouzloo, C. A.; McMahon, P. N.; Sridhar, S. Quantitative Contrast-Enhanced Mri with Superparamagnetic Nanoparticles Using Ultrashort Time-to-Echo Pulse Sequences. *Magn. Reson. Med.* **2015**, *74*, 431−441.
(40) Zhang, J.; Ring, H. L.; Hurley, K. R.; Shao, Q.; Carlson, C. S.; Idiyatullin, D.; Manuchehrabadi, N.; Hoopes, P. J.; Haynes, C. L.; Bischof, J. C.; Garwood, M. Quantification and Biodistribution of Iron Oxide Nanoparticles in the Primary Clearance Organs of Mice Using T1 Contrast for Heating. *Magn. Reson. Med.* **2016**, DOI: 10.1002/mrm.26394.
(41) Hildebrandt, B.; Wust, P.; Ahlers, O.; Dieing, A.; Sreenivasa, G.; Kerner, T.; Felix, R.; Riess, H. The Cellular and Molecular Basis of Hyperthermia. *Crit Rev. Oncol Hematol* **2002**, *43*, 33−56.
(42) Sapareto, S. A.; Dewey, W. C. Thermal Dose Determination in Cancer Therapy. *Int. J. Radiat. Oncol., Biol., Phys.* **1984**, *10*, 787−800.
(43) Alphandery, E.; Faure, S.; Seksek, O.; Guyot, F. o.; Chebbi, I. Chains of Magnetosomes Extracted from Amb-1 Magnetotactic Bacteria for Application in Alternative Magnetic Field Cancer Therapy. *ACS Nano* **2011**, *5*, 6279−6296.
(44) Dennis, C. L.; Jackson, A. J.; Borchers, J. A.; Hoopes, P. J.; Strawbridge, R.; Foreman, A. R.; van Lierop, J.; Gruttner, C.; Ivkov, R. Nearly Complete Regression of Tumors *via* Collective Behavior of Magnetic Nanoparticles in Hyperthermia. *Nanotechnology* **2009**, *20*, 395103.
(45) Balivada, S.; Rachakatla, R. S.; Wang, H.; Samarakoon, T. N.; Dani, R. K.; Pyle, M.; Kroh, F. O.; Walker, B.; Leaym, X.; Koper, O. B.; Tamura, M.; Chikan, V.; Bossmann, S. H.; Troyer, D. L. A/C Magnetic Hyperthermia of Melanoma Mediated by Iron(0)/Iron Oxide Core/Shell Magnetic Nanoparticles: A Mouse Study. *BMC Cancer* **2010**, *10*, 119.
(46) Zhang, S.; Li, J.; Lykotrafitis, G.; Bao, G.; Suresh, S. Size-Dependent Endocytosis of Nanoparticles. *Adv. Mater.* **2009**, *21*, 419−424.
(47) Righetti, M. C.; Salvetti, G.; Tombari, E. Heat Capacity of Glycerol from 298 to 383 K. *Thermochim. Acta* **1998**, *316*, 193−195.
(48) Segur, J. B.; Oberstar, H. E. Viscosity of Glycerol and Its Aqueous Solutions. *Ind. Eng. Chem.* **1951**, *43*, 2117−2120.

DOI: 10.1021/acsnano.7b01762
ACS Nano XXXX, XXX, XXX−XXX